Top Catal (2011) 54:334–348
DOI 10.1007/s11244-011-9662-5

ORIGINAL PAPER

Effect of Particle Size and Adsorbates on the L_3, L_2 and L_1 X-ray Absorption Near Edge Structure of Supported Pt Nanoparticles

Yu Lei · Jelena Jelic · Ludwig C. Nitsche · Randall Meyer · Jeffrey Miller

Published online: 15 February 2011

Abstract Pt nano-particles from about 1 to 10 nm have been prepared on silica, alkali-silica, alumina, silica-alumina, carbon and SBA-15 supports. EXAFS spectra of the reduced catalysts in He show a contraction of the Pt–Pt bond distance as particle size is decreased below 3 nm. The bond length decreased as much as 0.13 Å for 1 nm Pt particles. Adsorption of CO and H_2 lead to a increase in Pt–Pt bond distance to that near Pt foil, e.g., 2.77 Å. In addition to changes in the Pt bond distance with size, as the particle size decreases below about 5 nm there is a shift in the XANES to higher energy at the L_3 edge, a decrease in intensity near the edge and an increase in intensity beyond the edge. We suggest these features correspond to effects of coordination (the decrease at the edge) and lattice contraction (the increase beyond the edge). At the L_2 edge, there are only small shifts to higher energy at the edge. However, beyond the edge, there are large increases in intensity with decreasing particle size. At the L_1 edge there are no changes in position or shape of the XANES spectra. Adsorption of CO and H_2 also lead to changes in the L_3 and L_2 edges, however, no changes are observed at the L_1 edge. Density Functional Theory and XANES calculations show that the trends in the experimental XANES can be explained in terms of the states available near the edge. Both CO and H_2 adsorption result in a depletion of states at the Fermi level but the creation of anti-bonding states above the Fermi level which give rise to intensity increases beyond the edge.

Keywords Pt nanoparticles · Bond length contraction · Particle size effect in XANES spectra · Particle size effect in Pt bond length · Pt XANES · EXAFS

Y. Lei · J. Jelic · L. C. Nitsche · R. Meyer (✉)
Department of Chemical Engineering,
University of Illinois at Chicago, Chicago, IL 60607, USA
e-mail: rjm@uic.edu

J. Miller (✉)
Chemical Sciences and Engineering Division,
Argonne National Lab, Argonne, IL 60439, USA
e-mail: millerjt@anl.gov

1 Introduction

Metal clusters have been shown to demonstrate unique catalytic activity as their length scale is shrunk to the nanometer scale [1]. X-ray Absorption Near Edge Structure (XANES) and Extended X-ray Absorption Fine Structure (EXAFS) experiments have previously been employed in an effort to understand how the electronic and geometric structures of metal nanoparticles relate to their chemical reactivity [2, 3]. However, there are unresolved questions in the interpretation of XANES of metal nanoparticles and how particle size and adsorbates affect the XANES. Previous studies have noted differences in the edge intensity between supported nanoparticles and metal foil [4–7]. For example, in a series of Pt/SiO_2 catalysts with particle sizes ranging from 1.0 to 5.0 nm, Ichikuni and Iwasawa who found that the edge intensity at both the L_3 and L_2 edges of Pt changed as a function of particle size [6]. They interpreted the increase in intensity at the L_3 and L_2 edges as the particle size decreased as an indication of electron deficiency in Pt nanoparticles as compared to Pt foil. Although the work of Ichikuni and Iwasawa systematically established trends in the XANES for particle size of Pt, the origins of these changes in the edge are not well understood. In contrast, simulation work has not been able to elucidate trends observed experimentally. For example, Ankudinov et al. who found that the initial leading edge did

not vary significantly between Pt_{13} and Pt foil, suggesting that current scattering calculations are not sufficient to simulate the absorption experiments [8, 9].

More recently Schweitzer et al. have shown that the Pt edge intensity and position changes in Pt alloys and is dependent on the alloying metal [10]. For example, when Pt is alloyed with Sn, Pt L_3 XANES edge broadens and its intensity decreases compared to pure Pt. Density functional theory (DFT) calculations show that the *d*-band broadens and shifts away from the Fermi level leading to a lower density of states at the Fermi level. Based on the ground state electronic structure, Schweitzer et al., have calculated the oscillator strength of the electronic transition which is analogous to a simulated XANES. The shift to higher edge energy was interpreted to be correlated to a *d*-band center broadening (and shift). Conversely, in PtRu catalysts the XANES edge energy is shifted to lower energy as the *d*-band center narrows and shifts toward the Fermi level.

The presence of adsorbates such as hydrogen or CO on metals has also been observed to shift the XANES edge location and intensity [11–29]. Hydrogen has been found consistently to broaden the L_3 edge and shift it to higher energy [27]. Using the simple argument that the magnitude in the edge intensity is correlated with the number unoccupied *d* orbitals of Pt, early studies have argued that hydrogen effectively donates electron density to Pt [6, 11]. More recent studies have suggested that the change in magnitude and shape of the Pt L_3 edge after hydrogen adsorption can be thought of in terms of the creation of antibonding orbitals above the Fermi level which can now be accessed in an electron scattering event [12, 15, 16, 27]. Ramaker et al. [14] have further described features above the edge as a consequence of multiple scattering events. In addition, to hydrogen, other adsorbates such as CO [28, 29] and C_2H [22, 30] have been examined for their effect on the Pt XANES. However the theoretical explanation of the shifts in the edge intensity are almost all based upon FEFF calculations of the adsorbate on a 6 atom cluster. As has been discussed in Stoupin et al., this model does not allow for a complete description of the electronic structure of the metal nanoparticle and therefore, these calculations show strong sensitivity to the adsorption site [31].

Guo et al. have recently shown in a combined experimental and computational examination of competitive adsorption in Pt (and Au) water gas shift catalysts that the edge intensity and position can be shifted by the presence of adsorbates [32]. Shifts in the edge position where interpreted as a measure of the PDOS at (or near) the Fermi level as OH and CO lead to either a decrease or an increase in the edge energy, respectively. However, in both cases the edge intensity increased dramatically suggesting a more complex explanation is required. At this point, no general rules exist, however, for prediction of XANES shifts in either edge location or intensity.

In this study the Pt L_3 EXAFS and L_3, L_2 and L_1 XANES of supported Pt catalysts in He and with adsorbed CO and H_2 have been determined in order to examine the changes in structure and electronic properties with particle size on different supports (SiO_2, K–SiO_2, Al_2O_3, C, SiO_2–Al_2O_3 and SBA-15). DFT calculations were also performed in order to interpret these electronic changes and to establish relationships between the *d* electron PDOS and the XANES spectra.

2 Experimental

2.1 Catalyst Preparation

2.1.1 Pt/Silica

Pt/Silica A 80 g of Davisil 644 silica (Aldrich) was slurried in 500 mL H_2O and NH_4OH was added until the pH was about 10. 1.6 g of $Pt(NH_3)_4(NO_3)_2$ (PtTA) was dissolved in 200 mL H_2O, and the pH was adjusted to about 10 with NH_4OH. The PtTA solution was added rapidly to the silica, stirred for 30 min and filtered. The solid was washed 2 × 250 mL with cold H_2O, dried overnight at 125 °C and calcined at 200 °C. The catalyst was reduced at 250 °C by heating rapidly from room temperature to 150 °C in H_2 and holding for 30 min. The temperature was increased to 200 °C for 30 min and finally to 250 °C for 30 min. The catalyst was purged with He at 250 °C and cooled to room temperature. The elemental analysis was 0.99% Pt with a H/Pt of 0.89.

Pt/Silica B 0.50 g of PtTA was dissolved in 22 mL H_2O with addition of three drops of HNO_3. The PtTA solution was added to 20 g of Davisil 644 silica by incipient wetness impregnation and dried overnight at 125 °C. Half of catalyst was reduced following the procedure for Pt/silica A.

Pt/Silica C Half of Pt/silica B was calcined at 250 °C for 5 h in flowing air and reduced. The elemental analysis was 1.19% Pt.

Pt/SiO_2 D 0.90 g of PtTA was dissolved in 50 mL H_2O and added to 45 g of Davisil 644 silica by incipient wetness impregnation. The catalyst was dried overnight, and 5 g was calcined at 600 °C for 5 h. The catalyst was reduced identical to Pt/silica A. The elemental analysis was 1.05% Pt. The H/Pt was 0.10.

2.1.2 Pt/K–Silica

K–Silica support To 250 g of Davisil 644 SiO_2 in 2 L H_2O was added 4.0 g KOH dissolved in 500 mL H_2O giving a

pH of about 9. The slurry was stirred was for 1 h at 60 °C, filtered, washed 2 × 250 mL, and dried overnight at 125 °C.

Pt/K–Silica B To 50 g of K-Silica in 250 mL H_2O was added 2 mL NH_4OH to give a pH of about 10. 5.0 g PtTA was dissolved in 250 mL H_2O with 1 mL NH_4OH. The PtTA was added rapidly with stirring to the K–Silica. After 15 min the solid was filtered, washed 2 × 200 mL H_2O and dried at 125 °C overnight. The elemental analysis was 4.1% Pt. 10 g of catalyst was reduced following the procedure for Pt/silica A.

Pt/K–Silica A 10 g of Pt/K–Silica A was calcined in flowing air at 225 °C for 5 h and reduced identical to Pt/silica A.

Pt/K–Silica C 10 g of Pt/K–Silica A was calcined in flowing air at 300 °C for 5 h, and reduced identical to Pt/silica A.

2.1.3 Pt/SiO_2–Al_2O_3

Pt/SiO_2–Al_2O_3 A 80 g of Davison 135 SiO_2–Al_2O_3 was slurried in 300 mL H_2O. 1.60 g PtTA was dissolved in 75 mL H_2O (pH 5) and rapidly added to the support with stirring. After 30 min, the solid was filtered, washed 2 × 250 mL H_2O, and dried at 125 °C overnight. The elemental analysis was 0.54% Pt. The catalyst was reduced identical to Pt/silica A.

Pt/SiO_2–Al_2O_3 B 0.4 g of PtTA was dissolved in 22 mL H_2O with five drops of concentrated HNO_3 (pH 2). The PtTA solution was added to 20 g of Davison 135 SiO_2–Al_2O_3 by incipient wetness impregnation and dried overnight at 125 °C. The catalyst was reduced identical to Pt/silica A. The elemental analysis was 0.98% Pt.

Pt/SiO_2–Al_2O_3 C 80 g of Davison 135 SiO_2–Al_2O_3 was slurried in 300 mL H_2O and the pH was adjusted to about 10 with NH_4OH. 1.60 g PtTA was dissolved in 75 mL H_2O and rapidly added to the support with stirring. After 30 min, the solid was filtered, washed 2 × 250 mL H_2O, and dried at 125 °C overnight. The elemental analysis was 0.96% Pt. The catalyst was reduced identical to Pt/silica A. The H/Pt was 0.19.

2.1.4 Pt/Al_2O_3

Pt/Al_2O_3 A 1.50 g of PtTA was dissolved in 25 mL H_2O with addition of three drops of HNO_3. The PtTA solution was added to 50 g of Catalpal SB γ-Al_2O_3 by incipient wetness impregnation and dried overnight at 125 °C. Half of the catalyst was reduced by heating rapidly to 200 °C for 30 min. The temperature was increased to 250 °C for 30 min and finally to 300 °C for 30 min, purged with He at 300 °C and cooled to room temperature. The elemental analysis was 1.5% Pt.

Pt/Al_2O_3B 2.5 g of PtTA was dissolved in 23 mL H_2O with addition of three drops of HNO_3. The PtTA solution was added to 45 g of Catalpal SB γ-Al_2O_3 by incipient wetness impregnation and dried overnight at 125 °C. The catalyst was calcined at 450 °C in air for 5 h and reduced identical to Pt/Al_2O_3 A. The elemental analysis was 2.6% Pt.

Pt/Al_2O_3 C 1.3 g of H_2PtCl_6 was dissolved in 7.5 mL H_2O with five drops of concentrated HCl. The Pt solution was added to 15 g of Catalpal SB γ-Al_2O_3 by incipient wetness impregnation and dried overnight at 125 °C. The catalyst was reduced identical to Pt/Al_2O_3 A. The elemental analysis was 3.24% Pt.

Pt/Al_2O_3 D 0.75 g NH_4Cl was dissolved in 12 mL H_2O and added to 25 g of Pt/Al_2O_3 A by incipient wetness impregnation. The catalyst was dried overnight at 125 °C and calcined at 225 °C for 3 h in flowing air. The catalyst was reduced identical to Pt/Al_2O_3 A.

Pt/Al_2O_3 E 100 g of Catalpal SB γ-Al_2O_3 was calcined at 725 °C for 5 h. The surface area was 165 m^2/g. 1.50 g of PtTA was dissolved in 25 mL H_2O with addition of three drops of HNO_3. The PtTA solution was added to 50 g of calcined alumina by incipient wetness impregnation, dried overnight at 125 °C, and calcined at 250 °C for 3 h. 10 g of catalyst was reduced identical to that for Pt/Al_2O_3 A. The elemental analysis was 1.5% Pt and the H/Pt was 0.75.

Pt/Al_2O_3 F 10 g of Pt/Al_2O_3 E was calcined at 625 °C for 5 h and reduced. The H/Pt was 0.13.

2.1.5 Pt/C

Pt/C A 0.70 g of H_2PtCl_6 was dissolved in 12 mL H_2O and added to Vulcan Carbon (Cabot Corp) and dried at 135 °C. The catalyst was reduced by the method of Pt/silica A. The elemental analysis was 2.64% Pt.

Pt/C B 10 g of Timrex carbon (TIMCAL Graphite and Carbon) was slurried in 200 mL H_2O and the pH was adjusted to about 10 with NH_4OH. 0.40 g of PtTA was dissolved in 50 mL H_2O with 1 mL NH_4OH. The PtTA solution was added to the C slurry and stirred for 30 min, filtered, washed 2 × 250 mL with H_2O and dried at 135 °C. The elemental analysis was 1.67% Pt.

2.1.6 Pt/SBA-15

2 nm (*Pt/SBA-15 A*), 5 nm (*PtSBA-15 B*) and 9 nm (*Pt/SBA-5 C*) colloidal Pt nano-particles supported on SBA-15 were supplied by Rob Rioux and prepared by reduction of H_2PtCl_6 with alcohols and supported on SBA-15 as previously reported [33].

The elemental analysis of Pt was determined by inductively coupled plasma. Hydrogen chemisorption was

determined by the double isotherm method and the dispersion was calculated assuming a Pt/H ratio of 1.

3 STEM

Scanning Transmission Electron Microscopy (STEM) measurements were made on the reduced samples. Several milligrams of catalyst was mixed with iso-propanol and sonicated for 10 min. A drop of the slurry was deposited on a carbon-coated copper grid, (200 mesh, CuPK/100) from SPI suppliers, and thoroughly dried with an ultra infrared lamp. High angle annular dark field (HAADF) Z-contrast images were obtained on JEM-2010F FasTEMm FEI manufactured by JEOL and operated at 200 keV and extracting voltage of 4,500 V. Typically, ten different regions of a catalyst were imaged for particle size analysis and from 500 to 2000 particles were analyzed obtained using Particule2 software provided by Dr. Catherine Louis, University Pierre et Marie Curie in Paris, to determine the particle size distribution.

3.1 EXAFS and XANES Data Collection and Analysis

X-ray absorption measurements were made on the insertion-device beam line of the Materials Research Collaborative Access Team (MRCAT) at the Advanced Photon Source, Argonne National Laboratory. A cryogenically cooled double-crystal Si (111) monochromator was used in conjunction with an uncoated glass mirror to minimize the presence of harmonics. The monochromator was scanned continuously during the measurements with data points integrated over 0.5 eV for 0.07 s per data point. Full EXAFS spectra were obtained in quick scan mode in about 4 min. Measurements were made in transmission mode with the ionization chambers optimized for the maximum current with linear response ($\sim 10^{10}$ photons detected/s) using a mixture of nitrogen and helium in the incident X-ray detector and a mixture of ca. 20% argon in nitrogen in the transmission X-ray detector. A platinum foil spectrum was acquired simultaneously with each measurement for energy calibration. Pt–Pt Phase shift and backscattering amplitude functions were obtained from reference compounds: $Pt(NH_3)_4(NO_3)_2$ for Pt–O ($N_{Pt-N} = 4$ at 2.05 Å) and Pt foil and Pt–Pt ($N_{Pt-Pt} = 12$ at 2.77 Å). Standard procedures based on WINXAS software were used to extract the EXAFS data. The coordination parameters were obtained by a least square fit in q- and r-space of the isolated, k^2-weighted Fourier transform data. The quality of the fits were equally good with both k^1 and k^3 weightings. The coordination numbers were converted to particle sizes via the following formula developed by Miller et al. [34]:

$$\log_{10}(1000/\mathrm{d}) = 2.5763 - 0.1319 \times (\mathrm{CN})$$

Catalyst samples were pressed into a cylindrical holder, which could simultaneously hold six samples, and placed into a controlled atmosphere cell equipped with shut-off valves to isolate the sample after pre-treatment. The sample thickness was chosen to give a total absorbance at the Pt L_3 (11.564 keV), L_2 (13.273 keV) and L_I (13.892 keV) edges between 1 to 2 and edge step of at least 0.4. The catalysts were reduced at 250 °C at atmospheric pressure in 4% H_2/He at 150 cc/min. Trace oxidants in He were removed by passing through a Matheson PUR-Gas Triple Purifier Cartridge. After reduction, the samples were purged with He at 100 cc/min for 15 min at 250 °C and cooled to room temperature in He flow. Pt L_3 EXAFS and L_3, L_2 and L_1 XANES spectra were obtained at room temperature in He. Following data collection on the reduced catalysts, the samples were saturated for 15 min at 100 cc/min with either 4% H_2 or 1% CO at room temperature, followed by 15 min He purge. Additional L_3 EXAFS and L_3, L_2 and L_1 XANES spectra were obtained on the catalysts with adsorbed H_2 or CO at room temperature. Additionally, the Pt L_3 EXAFS were obtained at 250 °C in He on several reduced catalysts. The Debye–Waller factor is temperature dependent and the value at 250 °C was determined by fitting some catalysts at room temperature and 250 °C assuming the same coordination number at both temperatures.

3.2 Density Functional Theory Calculations/XANES Simulations

The DFT calculations in this work are performed using the CASTEP Package [35]. A plane-wave basis set with a cutoff energy of 500 eV and ultra-soft Vanderbilt pseudopotentials (US-PP) [36] was used in all calculations reported herein. All calculations are carried out with 1×1 unit cell of a 4 layer Pt(111) slab with a $8 \times 8 \times 1$ Monkhorst–Pack kpoint grid [37]. The upper two layers of the Pt(111) surface are relaxed in the slab calculations. Vacuum space equivalent to 4 atomic layers of Pt was used to separate the slabs. Within CASTEP a module exists for simulation of XANES/EELS spectra. The Perdew–Wang (PW-91) form of the exchange and correlation functional was used within the generalized gradient approximation (GGA) [38]. Although the specifics of using the CASTEP pseudopotential DFT code to calculate XANES spectra are given in more detail in the work of Gao et al. [39, 40] and Seabourne et al. [41], we will briefly summarize the method here. The EELS spectra are determined from the transition matrix elements between the core state and a pseudowavefunction of the final state which is then corrected for differences between the pseudo-wave function and the all electron calculation via a projector augmented

wave reconstruction. The core state is evaluated using an all electron calculation of an isolated atom whereas the pseudowavefunction of the final state is generated by an ultrasoft pseudopotential calculation within CASTEP. Since spin coupling energy is not included in the Hamiltonian, we cannot differentiate between the L_2 and L_3 edges. Calculations were performed without the inclusion of a core hole due to the electron shielding of core states although calculations were also carried out including the core hole to confirm its effect, which was found to be insignificant. Gaussian broadening of 3.0 eV is applied to mimic the instrument broadening, and the fact that calculations necessarily involve a finite number of k-points [40]. A more detailed discussion of the key considerations for calculating the EELS/XANES using CASTEP is provided by Seaborne et al. [41].

The effect of adsorbates on the XANES spectra was examined by placing the adsorbate in its lowest energy configuration (CO [42] and H sit in the fcc site) and all calculations were performed with a coverage of 1.0 ML (an artificially high coverage designed to exacerbate the effect of the adsorbate). As will be discussed below, this allows for a qualitative comparison between the experimental spectra and those we have calculated.

A Pt_6 octahedron was also examined as a means of investigating the effect of the particle size on the XANES spectra. It should be noted that multiple structures may exist for Pt_6 [43] and we have made no attempt to address deformations that may occur for supported clusters [44]. Instead, we have chosen a frequently studied structure which represents a local minimum and is chosen for elucidation of qualitative trends. When examining the Pt_6 clusters all atoms were allowed to fully relax.

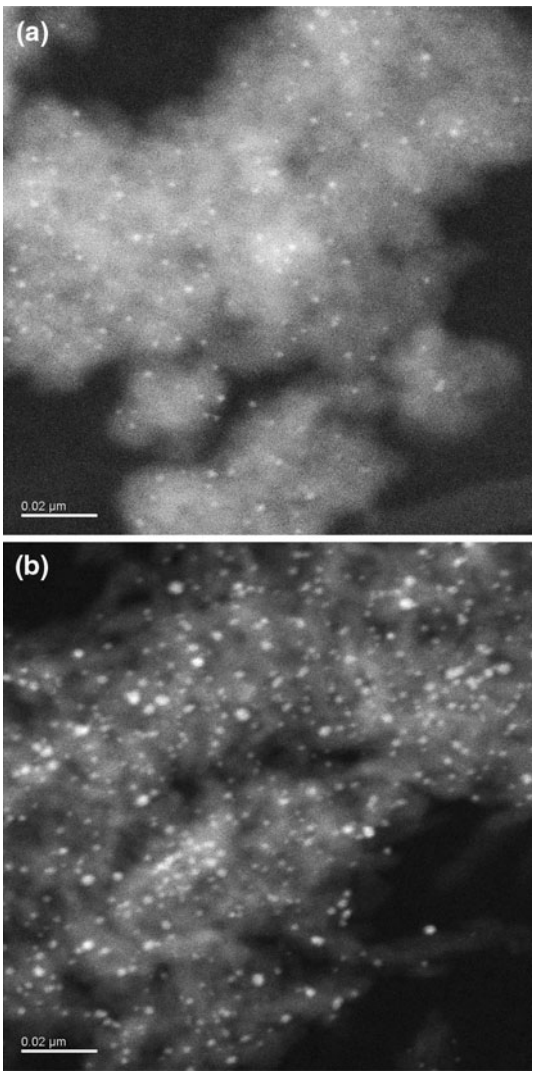

Fig. 1 STEM of **a** 4.0% Pt/K–SiO_2 A (average size 1.5 nm); *scale bar* = 0.02 µm. **b** 3.2% Pt/Al_2O_3 C (average size 2.0 nm); *scale bar* = 0.02 µm

4 Results

Platinum catalysts have been prepared on different supports, silica, alkali-silica, silica-alumina, alumina, carbon and SBA-15. By varying the platinum salt, solution pH, method of metal deposition and calcination temperature, the Pt particle size was varied. The catalyst particle size was determined by a combination of dark field STEM, hydrogen chemisorption and EXAFS spectroscopy. Typical dark field STEM images are shown in Fig. 1a and b for Pt/K–SiO_2 A and Pt/Al_2O_3 C, respectively. For Pt/K–SiO_2 A, the particle size distribution (not shown) indicates an average size of 1.5 nm with about 5% of the particles larger than 2.0 nm. Similarly, the average particle size on Pt/Al_2O_3 C was 2.0 nm with less than 5% of particles larger than 2.8 nm. A summary of the average particle size by STEM is given in Table 1.

Additional information on the Pt particle sizes was determined by EXAFS spectroscopy at room temperature after the catalysts were reduced in 4% H_2/He at 300 °C for 30 min. The first-shell EXAFS spectra were obtained by a Fourier transform of the k^2-weighted data from 2.75 to 12.2 $Å^{-1}$. The fit parameters were determined by fitting both the magnitude and imaginary parts of the Fourier transform of the isolated k^2-weighted EXAFS spectra and are summarized in Table 1. Assuming hemispherical nanoparticles, estimates of the average sizes were determined based on previous correlations of the N_{Pt-Pt} with dispersion [34] and are also given in Table 1. There is good agreement of the sizes determined by EXAFS, STEM and hydrogen chemisorption.

Additional EXAFS spectra were obtained for several catalysts reduced at 250 °C. Since the Debye–Waller factor

Table 1 L_3 EXAFS fits of Pt catalysts reduced 300 °C and in He at RT

% Pt	Support	N_{Pt-Pt}	R (Å)	DWF ($\times 10^3$)	E_o (eV)	XAS Est. size (nm)	TEM size (nm)
1.0	SiO_2 A	5.0	2.69	2.0	−5.1	1.2	1.4
1.2	SiO_2 B	6.2	2.72	2.0	−3.0	1.7	1.7
1.2	SiO_2 C	7.1	2.73	1.5	−2.9	2.3	2.4
4.0	K–SiO_2 A (0.3% K)	5.0	2.70	2.0	−3.3	1.2	1.5
4.0	K–SiO_2 B (0.3% K)	5.5	2.70	2.0	−3.6	1.4	1.6
4.0	K–SiO_2 C (0.3% K)	6.2	2.73	2.0	−2.6	1.7	1.7
1.5	Al_2O_3 A	4.2	2.64	2.5	−7.6	0.9	nd
2.6	Al_2O_3 B	5.0	2.68	2.0	−5.1	1.2	1.8
3.2	Al_2O_3 C	6.4	2.72	2.0	−3.6	1.9	2.0
1.5	Al_2O_3 D	9.6	2.75	1.5	−2.4	5.0	nd
0.5	SiO_2–Al_2O_3 A	3.9	2.64	2.5	−6.9	0.9	nd
1.0	SiO_2–Al_2O_3 B	5.3	2.69	2.0	−4.9	1.3	1.5
1.0	SiO_2–Al_2O_3 C	7.8	2.74	1.5	−3.4	2.8	2.6
2.6	Carbon A	4.6	2.67	2.5	−7.5	1.1	1.4
1.7	Carbon B	7.0	2.73	2.0	−3.6	2.2	2.2

(DWF) is temperature dependent, after collecting the spectrum at 250 °C on the Pt/C B catalyst, an additional spectrum was collected at room temperature. The coordination number determined from the room temperature fit was assumed to be unchanged at high temperature to determine the DWF at 250 °C. The remaining catalysts were fit using this DWF value. The fit parameters and particle size estimates for the catalysts at 250 °C are given in Table 2. In addition to catalysts prepared by standard solution methods and thermal treatments, 2, 5 and 9 nm Pt nanoparticles were prepared using SBA-15 via colloidal methods described in the experimental section above [33]. The advantage of this method is that it gives a more uniform size distribution than traditional solution syntheses, especially for larger particle sizes.

The fit results in Tables 1 and 2 show that for catalysts in He the Pt–Pt bond distances are shorter than bulk Pt (2.77 Å). Figure 2 shows the Fourier transform for representative data of two of the catalysts (2 and 5 nm colloidal Pt nanoparticles on SBA-15). As can be observed in Fig. 2, as the size of the nanoparticle gets smaller, the peaks in the magnitude of the Fourier transform for the first shell Pt–Pt distance, (located between about 1.7 and 3.1 Å), get smaller. The peak size in the Fourier transformed spectra is proportional to the coordination number (i.e. a measure of particle size). In addition, there is a shift to lower R and indicating a significant decrease in the Pt–Pt bond distance.

Figure 3 shows a correlation of the Pt–Pt first shell bond distance with particle size for all catalysts. All particles smaller than about 10 nm show a contraction in the first shell Pt–Pt bond distance; the contraction decreases rapidly for sizes smaller than about 4 nm and is very similar to that to previous observations of Pt nanoparticles [45], as well as for Au nanoparticles [34] and Pd nanoparticles [46]. At about 1 nm, the decrease in bond distance is 0.13 Å, e.g., 2.77 Å in Pt foil and 2.64 Å for 1 nm Pt nanoparticles. Although Frenkel et al. have noted the contraction of Pt–Pt bonds with increasing temperature [30, 47], we find that the contraction in bond distance is identical at room temperature and 250 °C. As shown below, the Pt–Pt bond distance is also dependent on the presence of adsorbates and was recently shown to continuously change with surface coverage [5]. Thus, the decreasing bond distance with increasing temperature of Frenkel, may be due to a

Table 2 L_3 EXAFS fits of Pt catalysts reduced 250 °C and in He at 250 °C

% Pt	Support	N_{Pt-Pt}	R (Å)	DWF ($\times 10^3$)	E_o (eV)	XAS Est. size (nm)	TEM size (nm)
1.0	SiO_2 D	11.0	2.76	4.5	−1.8	7.5	Nd
1.5	Al_2O_3 E	4.8	2.66	4.5	−5.8	1.2	Nd
1.5	Al_2O_3 F	11.7	2.77	4.5	−1.2	9.0	Nd
1.7	Carbon B	6.5	2.72	4.5	−4.8	2.0	2.2
1.0	SBA-15 A	5.2	2.65	4.5	−4.5	1.3	1.5
1.0	SBA-15 B	9.8	2.75	4.5	−2.9	5.0	5.0
1.0	SBA-15 C	11.5	2.76	4.5	−2.4	8.5	9.0

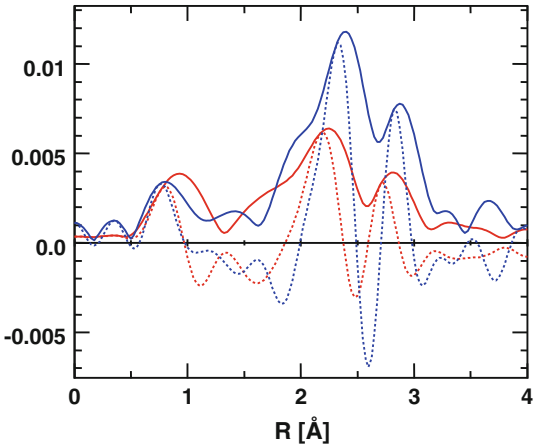

Fig. 2 Comparison of the Fourier transform for reduced 2 nm (Pt/SBA-15 A) and 5 nm (Pt/SBA-15 B) Pt particles on SBA-15 at 250 °C in He. (k^2: $\Delta k = 2.8$–11.7 Å^{-1}; *solid line* magnitude of FT and *dotted line* imaginary part FT). *Red* Pt/SBA-15 A ($N_{Pt-Pt} = 5.2$, $R = 2.65$ Å). *Blue* Pt/SBA-15 B ($N_{Pt-Pt} = 9.8$, $R = 2.76$ Å)

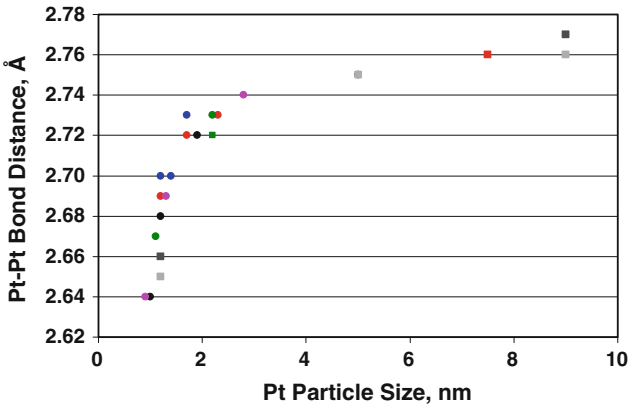

Fig. 3 Correlation of metallic Pt nano-particle size with Pt–Pt bond distance in He (*red* Pt/silica, *blue* Pt/K–silica, *black* alumina, *pink* silica–alumina, *green* carbon and *gray* SBA-15; *circle* room temperature and *square* at 250 °C)

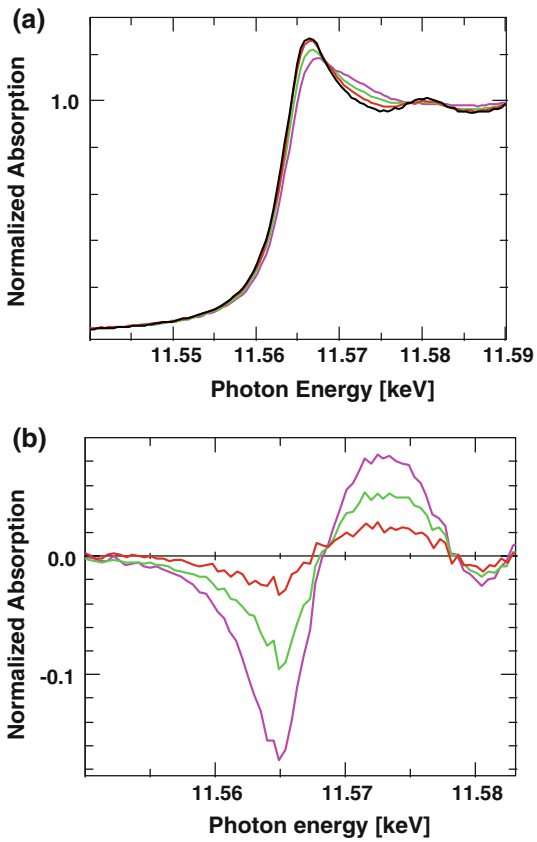

Fig. 4 **a** Pt L_3 XANES from 11.54 to 11.59 keV for Pt/Alumina catalysts in He. *Pink* Pt/Al_2O_3 A (0.9 nm). *Green* Pt/Al_2O_3 B (1.2 nm). *Red* Pt/Al_2O_3 D (5.0 nm). *Black* Pt Foil. **b** Pt L_3 ΔXANES (catalyst XANES in He–XANES Foil) from 11.55 to 11.583 keV for Pt/Alumina catalysts. *Pink* Pt/Al_2O_3 A (0.9 nm). *Green* Pt/Al_2O_3 B (1.2 nm). *Red* Pt/Al_2O_3 D (5.0 nm)

decrease in hydrogen surface coverage at elevated temperature. The lattice contraction is essentially independent of the support, implying that epitaxial growth on the underlying support is not a requirement for the lattice contraction and that this phenomenon is general across a large variety of substrates. Density functional theory calculations also reproduce this decrease in the average bond distance from the bulk (chosen to mimic large particles) distance of 2.81 Å down to 2.71 Å for a Pt_{13} icosahedron.

In addition to decreases in the Pt–Pt bond distance with decreasing particle size, there are also changes in the XANES spectra (in He). Figure 4a shows the changes of the L_3 edge with decreasing particle size for Pt/alumina. As the particle size decreases below about 5 nm there is a decrease in intensity near the edge and an increase in intensity beyond the edge. The changes in the XANES increase as the particle size decreases below about 2 nm. Nearly identical behavior has been observed by Tew et al. recently for the L_3 edge of Pd catalysts on various supports [48]. Previous studies have not always provided a consistent answer to the effect of particle size on XANES as some authors have found an increase in the L_3 edge intensity as particle size decreases [5, 6]. However, a number of studies have demonstrated similar behavior as our observations here even if the experiments were not performed for a large number of samples with varying size [16, 49, 50].

The differences in the shapes of the XANES compared to the L_3 edge of Pt foil are shown in the difference XANES in Fig. 4b. The difference XANES, or ΔXANES, is determined by subtraction of the XANES spectrum of Pt foil from that of the catalyst. The decrease in intensity below the inflection point reflects a shift to higher energy at the edge, and the increase in the intensity above the inflection point is proportional to the increased intensity beyond the edge.

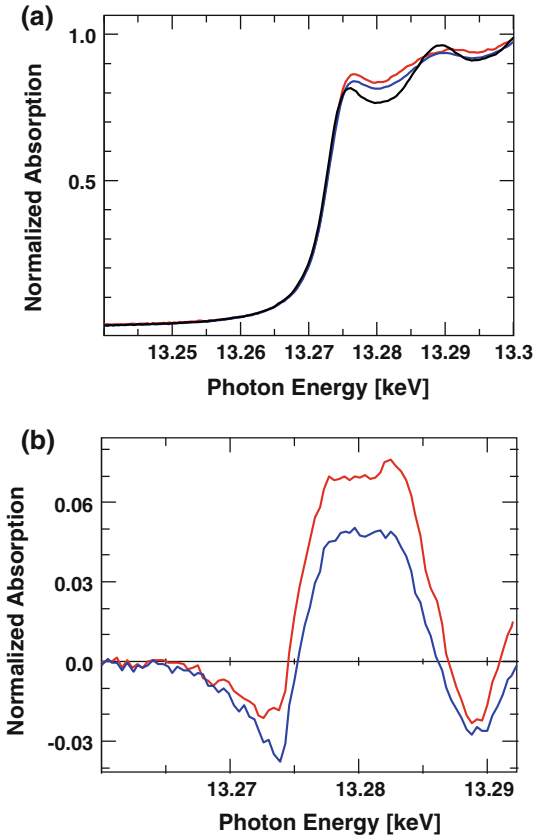

Fig. 5 **a** Pt L_2 XANES from 13.24 to 13.30 keV for Pt/Carbon catalysts in He. *Red* Pt/C A (1.1 nm). *Blue* Pt/C B (2.2 nm). *Black* Pt Foil. **b** Pt L_2 ΔXANES (catalyst XANES in He–XANES Foil) from 11.55 to 11.583 keV for Pt/Carbon catalysts. *Red* Pt/C A (1.1 nm). *Blue* Pt/C B (2.2 nm)

Typical changes in the intensity of the L_2 XANES with particle size are shown in Fig. 5a. At the L_2 edge, there are only small shifts to higher energy at the edge. However, beyond the edge, there is an increase in intensity with decreasing particle size. The L_2 ΔXANES spectra are shown in Fig. 5b. The data show a small decrease in the intensity at the absorption edge which increases slightly with increasing size with little variation among supports. In addition, above the edge there is much larger increase in XANES intensity that decreases with increasing particle size. These changes are independent of the support.

While there are significant changes in the Pt L_3 and L_2 XANES spectra with particle size, at the L_1 edge there are no changes in XANES edge position or shape with changing particle size. Figure 6 shows the L_1 XANES spectra of 0.8 nm Pt/SiO_2–Al_2O_3, 1.2 nm Pt/SiO_2 A and 1.7 nm Pt/SiO_2 B. No changes in the intensity of the L_I edge were observed for any particle size, or support type for particles smaller than about 2 nm. Small increases in the L_1 XANES intensity were observed for sizes larger than about 2 nm, however, this resulted from the overlap of the L_2 EXAFS at the L_1 edge.

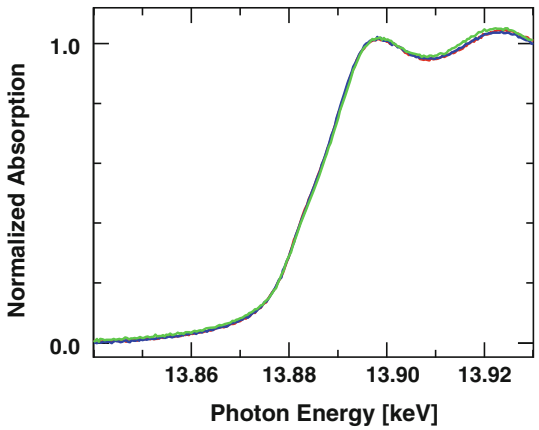

Fig. 6 Pt L_1 XANES from 13.83 to 13.94 keV for catalysts of different size in He. *Red* Pt/SiO_2–Al_2O_3 A (0.8 nm). *Blue* Pt/SiO_2 A (1.2 nm). *Green* Pt/SiO_2 B (1.7 nm)

4.1 The Effect of Adsorbed CO and H_2

In an effort to further investigate the behavior of small metal particles, we also examined the particles after exposure to CO and H_2 at room temperature. Adsorption of CO and H_2 on the Pt nanoparticles leads to a significant increase in bond distance for all sizes, Table 3. For nanoparticles larger than about 1.5 nm ($N_{Pt–Pt}$ greater than about 5), saturation with H_2 and CO give bond distances that are nearly identical to that in bulk. For the very smallest nanoparticles, even with adsorbates, the Pt–Pt bond distance is shorter than bulk; nevertheless, even for these 1 nm particles, the bond distance significantly increases with saturation coverage of these adsorbates. The increase in bond distance with adsorbates indicates that the Pt–Pt bond distance is dynamic and has been shown to vary linearly with the surface coverage [32].

As observed in several previous studies [14, 15, 27, 51], adsorption of CO and H_2 also leads to changes in the shape of the Pt L_3 and L_2 XANES spectra. Figure 7 shows the typical changes in Pt L_3 for Pt/Al_2O_3 catalysts of different size with adsorbed CO and H_2. As the particle size decreases, for both CO (Fig. 7a) and H_2 (Fig. 7b) there is a continual shift in the edge position to higher energy and increase in the intensity of the XANES compared to Pt foil. Similar behavior has also been observed on Pd catalysts when exposed to hydrogen [48].

Figure 8 shows similar changes in the L_2 XANES spectra for Pt/C of different size with adsorbed CO. Different from the L_3 edge, there is little shift in the position of the L_2 edge up adsorption of CO; however, there is a large increase in intensity with decreasing size beyond the edge.

Since the shape of the L_3 and L_2 XANES change with size as well as with the presence of an adsorbate, in order to determine the shape of these changes on the XANES due to

Table 3 L_3 EXAFS fits of Pt catalysts reduced 300 °C and at RT with adsorbed CO or H_2

% Pt	Support	Adsorbed gas	N_{Pt-Pt}	R (Å)	DWF ($\times 10^3$)	E_o (eV)
1.0	SiO_2 A	None (He)	5.0	2.69	2.0	−5.1
		H_2	5.4	2.75	1.0	−2.7
1.2	SiO_2 C	None (He)	7.1	2.73	1.5	−2.9
		H_2	7.4	2.76	1.0	−1.0
4.0	K–SiO_2 A (0.3% K)	None (He)	5.0	2.70	2.0	−3.3
		CO	4.7	2.76	1.0	−2.9
4.0	K–SiO_2 C (0.3% K)	None (He)	6.2	2.73	2.0	−2.6
		CO	6.0	2.76	1.0	−3.3
		H_2	6.4	2.76	1.0	−2.2
1.5	Al_2O_3 A	None (He)	4.2	2.64	2.5	−7.6
		H_2	4.1	2.69	1.0	−5.6
2.6	Al_2O_3 B	None (He)	5.0	2.68	2.0	−5.1
		CO	4.4	2.72	1.0	−5.5
		H_2	4.8	2.71	1.0	−5.7
3.2	Al_2O_3 C	None (He)	6.4	2.72	2.0	−3.6
		CO	6.0	2.74	1.0	−4.1
		H_2	6.4	2.74	1.0	−4.0
1.5	Al_2O_3 D	None (He)	9.8	2.74	1.5	−2.4
		CO	8.9	2.75	1.0	−2.9
		H_2	9.3	2.76	1.0	−2.6
1.0	SiO_2–Al_2O_3 C	None (He)	7.8	2.73	1.5	−3.4
		CO	7.5	2.76	1.0	−2.6
		H_2	7.7	2.74	1.0	−2.9
1.7	Carbon B	None (He)	7.0	2.73	2.0	−3.6
		CO	6.4	2.76	1.0	−1.9
		H_2	6.7	2.75	1.0	−2.6

the adsorbates it is necessary to compare the XANES of the catalysts in He and that with the adsorbate present. The ΔXANES, XANES of the catalysts with the adsorbate minus that in He, is shown in Fig. 9a and b for CO on Pt/Al_2O_3 and Pt/C, respectively. At both edges, the changes in shape are similar for both sizes and differ in intensity and reflect changes in the amount of adsorbed CO, i.e., changes in dispersion [32].

While there are significant changes in the Pt L_3 and L_2 XANES spectra with adsorbates, at the L_1 edge there are no changes in XANES edge position or shape with adsorbed CO or H_2. Figure 10 shows the L_1 XANES spectra of 1.2 nm Pt/K–SiO_2 A without adsorbate, e.g., He, and with adsorbed CO and H_2. Within experimental error these are identical.

5 Discussion

Recently, Linic and coworkers have used density functional theory based density of states calculations in order to understand electron energy-loss near edge structure (ELNES) [52]. Based upon the density of states and a transmission function for scattering from the 2*p* to the 3*d* of Ni determined from the earlier work of Muller et al. [53], a simulated ELNES spectrum was created that closely matched the experimental spectra. The formation of a surface alloy of Sn and Ni led to broadening of unoccupied Ni *d* states above the Fermi level due to hybridization of the Sn *s* and *p* states and the Ni *d* states. Several researchers have drawn parallels between electron energy loss spectroscopy and X-ray absorption near edge spectroscopy [54–56]. More recently, Schweitzer et al. had found for PtCu, PtRu and Pt_3Sn alloys that the integrated number of states under the edge did not change significantly, implying that charge transfer is not a dominant effect in these Pt alloy systems in agreement with prior work on Ni alloy systems [10]. Therefore, following a similar procedure, we calculated the density of unoccupied states near the Fermi level to explain the results of our XANES measurements.

Figure 11a shows the partial density of states of Pt_6 cluster and a Pt(111) slab. The *d*-electron density of states profile for the Pt_6 cluster is considerably narrower with more density near the Fermi edge than that for the Pt(111)

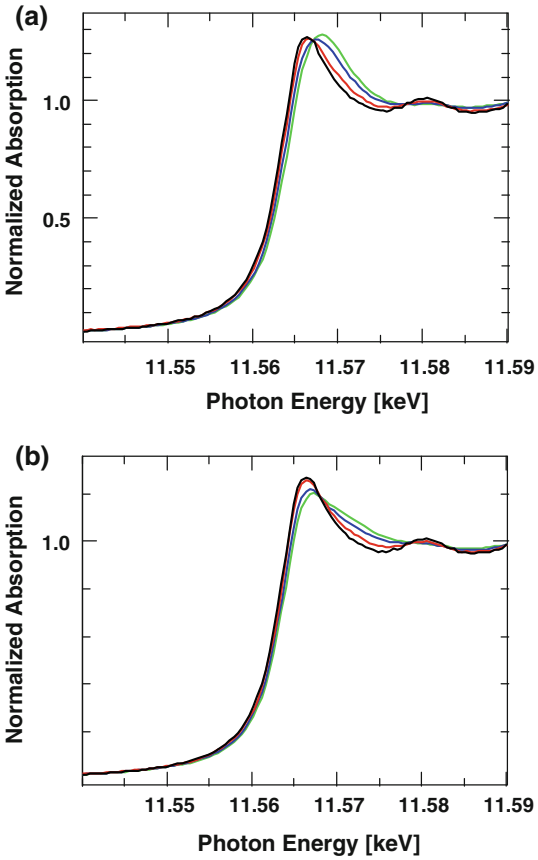

Fig. 7 **a** Pt L_3 XANES from 11.54 to 11.59 keV for Pt/Alumina catalysts with adsorbed CO. *Green* Pt/Al_2O_3 B (1.2 nm). *Blue* Pt/Al_2O_3 C (1.9 nm). *Red* Pt/Al_2O_3 D (5.0 nm). *Black* Pt Foil. **b** Pt L_3 XANES from 11.54 to 11.59 keV for Pt/Alumina catalysts with adsorbed H_2. *Green* Pt/Al_2O_3 B (1.2 nm). *Blue* Pt/Al_2O_3 C (1.9 nm). *Red* Pt/Al_2O_3 D (5.0 nm). *Black* Pt Foil

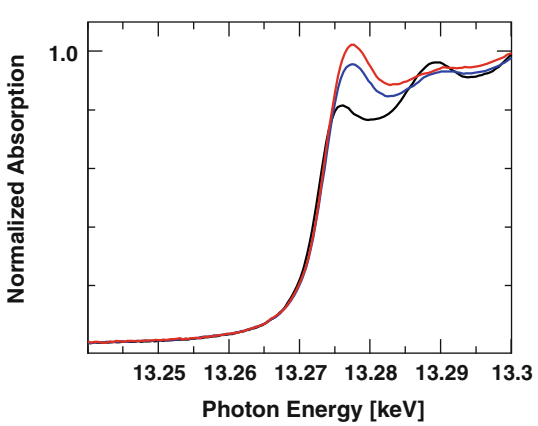

Fig. 8 Pt L_2 XANES from 13.24 to 13.30 keV for Pt/Carbon catalysts with adsorbed CO. *Red* Pt/C A (1.1 nm). *Blue* Pt/C B (2.2 nm). *Black* Pt Foil

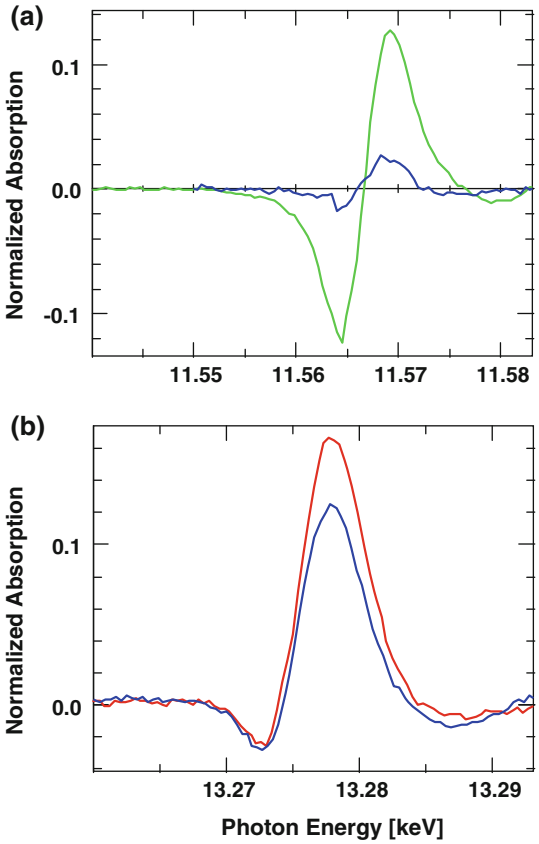

Fig. 9 **a** Pt L_3 ΔXANES (XANES with CO–XANES in He) from 11.55 to 11.583 keV for Pt/Alumina catalysts with adsorbed CO. *Green* Pt/Al_2O_3 B (1.2 nm). *Red* Pt/Al_2O_3 D (5.0 nm). **b** Pt L_2 ΔXANES (XANES with CO–XANES in He) from 13.26 to 13.293 keV for Pt/Carbon catalysts with adsorbed CO. *Red* Pt/C A (1.1 nm). *Blue* Pt/C B (2.2 nm)

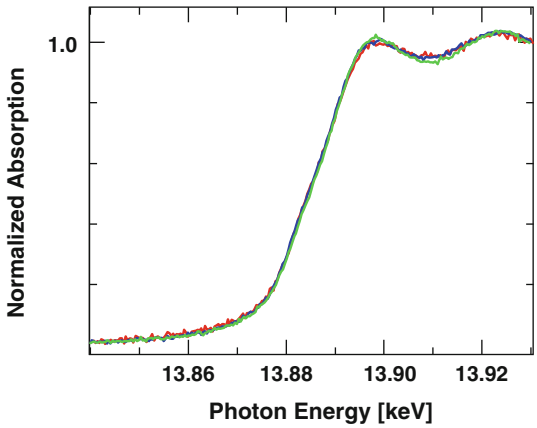

Fig. 10 Pt L_1 XANES from 13.83 to 13.94 keV for Pt/K–Silica A (1.2 nm) in He, H_2 and CO. *Red* $Pt/K–SiO_2$ A in He. *Blue* $Pt/K–SiO_2$ A with adsorbed H_2. *Green* $Pt/K–SiO_2$ A with adsorbed CO

slab. Concomitant to the narrowing of the *d*-band, the center of the *d*-band shifts toward the Fermi level (the *d*-band center shifts from −2.61 to −2.25 eV). The shift in the *d*-band center is a consequence of the need for a constant level of *d*-band filling in the metal, as has been explained by Norskov and Hammer [57, 58].

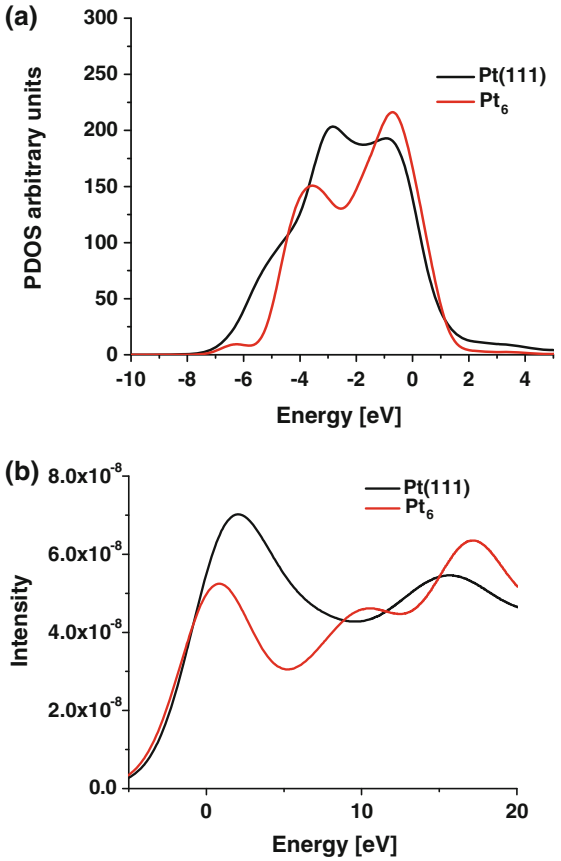

Fig. 11 **a** PDOS of Pt_6 and Pt(111). *Red* Pt_6. *Black* Pt(111). **b** Simulated XANES of Pt_6 and Pt(111). *Red* Pt_6. *Black* Pt(111)

Before we attempt to interpret our spectra at the L_3 edge, it is important to consider also the trend at the L_2 edge. While the XANES intensity decreases at the L_3 with decreasing particle size, the opposite trend is observed at the L_2 edge. There are two implications of this observation. First, the balance between the L_3 and L_2 is consistent with the notion that the total number of the *d* electrons is not a function of particle size. Second, due to changes in the bonding hybridization as the particle size decreases, the allowed transitions change. As Ramaker et al. note, the differences between the L_3 and L_2 edges reflect the fact that at the L_3, the $2p^{3/2}$ core electron may be promoted to either the $5d^{5/2}$ or $5d^{3/2}$ whereas the $2p^{1/2}$ at the L_2 can only be scattered to the $5d^{3/2}$ [14]. Ramaker et al. go on to analyze the difference between the L_3 and L_2 spectra as a ΔVB or change in the number of holes in the valence band. However, this analysis relies on the assumption of complete filling of the $5d^{3/2}$ as well as the alignment of edges based upon a particular ratio of the edge heights. This method does not seem to provide a consistent approach since the edge heights do not respond in a symmetric manner toward changes in oxidation state (as shown, for example in Zhao et al. [59].) or in response to adsorbates as discussed below. Unfortunately, in our current study, spin orbit coupling is not included in the simulated XANES so we cannot address this issue directly.

In our simulated XANES, we find that Pt clusters follow the same trend as the L_3 initial leading edge of the XANES intensity decreases with decreasing particle size as shown in Fig. 11b. Ankudinov et al. suggest that the integrated area under the edge is proportional to the number of localized *d* states above the Fermi level [60]. Previously, van Bokhoven and Miller have found that small gold particles had an increase in *d*-electron density at the L_3 edge relative to bulk gold [61]. FEFF calculations indicate that there is a small increase in the number of *d*-electrons in the smallest nanoparticles [34, 61]. The increase in *d*-electron density with decreasing coordination number has been interpreted as a decrease in the amount of *spd* hybridization in small gold clusters [62]. As the number of metal–metal bonds is reduced in small nanoparticles, the hybridization changes, resulting in a loss of *d*-band holes and, therefore, a loss of XANES intensity. The hybridization is a function of both the coordination (which for a surface atom in Pt_6 has decreased from 9 to 4) and Pt–Pt bond distance. The coordination effect has previously been used to explain the decrease in intensity at the edge for small particles [50]. As noted above, as the particle size is decreased, the Pt–Pt bond distance decreases dramatically (our Pt_6 cluster has an average bond length of 2.62 Å as compared to 2.81 Å for our Pt(111) slab) as has been shown previously by Ankudinov et al. [9]. The lattice contraction has been linked to a change in the hybridization of metal bonds as the particle seeks to minimize its under coordination [63]. Freund and co-workers have shown that the lattice contraction also contributes to binding energy shifts in X-ray Photoelectron Spectroscopy [64]. In small particles a competition exists between positive binding energy shifts (i.e. to higher binding energy; away from the Fermi edge) due to lattice contraction and negative binding energy shifts (i.e. toward the Fermi edge) due to the decrease in the average coordination number (from the increase in the percentage of surface atoms). In their calculations, Freund and co-workers find the degree of pure *d*–*d* bonding increases as the as the metal–metal bond distance and particle size decrease.

In an effort to understand the effect of lattice contraction, we have calculated the simulated XANES and PDOS for Pt(111) slabs whose average bond distance has been perturbed by ±5%. Previous calculations from Norskov and co-workers have shown that as the lattice is expanded in *d*-band transition metals, the *d*-band center moves toward the Fermi edge (from −2.60 to −2.22 eV) and conversely under contraction, the *d*-band center moves away from the Fermi edge (now to −3.09 eV) as show in Fig. 12a. The PDOS for *d* orbitals of Pt shows that the

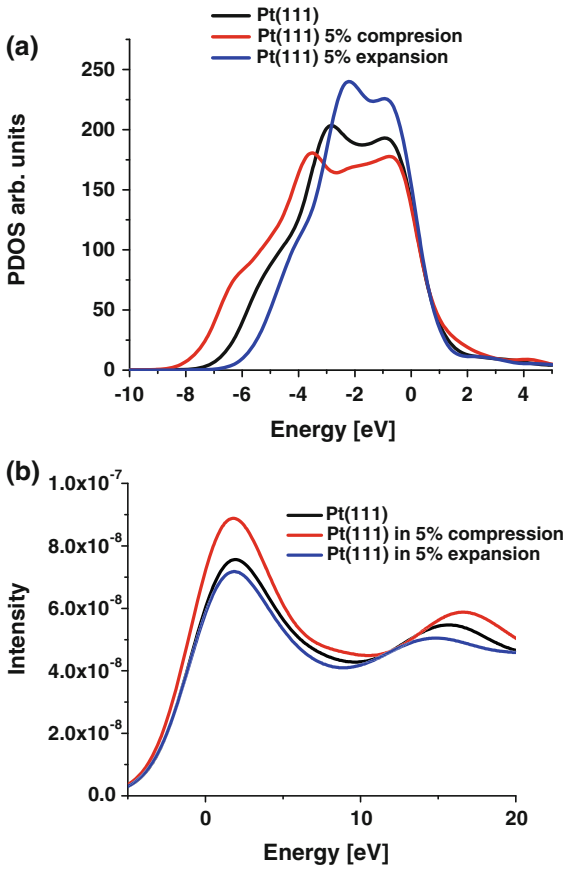

Fig. 12 **a** PDOS of Pt(111) under 5% expansion and compression. *Blue* Pt(111) expansion. *Red* Pt(111) compression. *Black* Pt(111). **b** Simulated XANES Pt(111) under 5% expansion and compression. *Blue* Pt(111) expansion. *Red* Pt(111) compression. *Black* Pt(111)

empty states are more diffuse for the contracted lattice. The simulated XANES of Pt(111), Pt(111) with 5% compression and Pt(111) with 5% expansion are shown in Fig. 12b. When the lattice is expanded, the degree of bonding is decreased and, therefore, more pure *d*-states exist resulting in a decrease in the XANES intensity. Conversely, as discussed above, when the lattice is contracted more *d* states participate in the metal–metal bonding leading to an increase in the available empty states above the edge. Therefore, we attribute the initial decrease in the edge intensity with decreasing particle size as an effect of coordination whereas the increase in intensity beyond the edge with decreasing particle size is related to lattice contraction in the small nanoparticles. Boyanov and Morrison have previously suggested that the presence of multiple features in the near edge region could be tied to the presence of spin orbit splitting in the Pt 5*d* states [65]. It is noteworthy that our calculation which does not include spin orbit coupling still captures the peak shapes from a qualitative standpoint.

Unlike the case for particle size effects, we observe that the intensity at both the L_3 (Fig. 8a) and L_2 (Fig. 7) edges increased dramatically when CO was adsorbed on the catalysts. The increase in XANES intensity after adsorption of CO could be interpreted as a charge transfer event. The Blyholder model would suggest that metal *d*-electron density is transferred to the CO π^* orbitals [66]. The increase in XANES intensity, therefore, would reflect the number of electrons involved with M–CO bond formation and the chemisorption bond energy. Looking at a Bader charge analysis of the system [67], some charge is transferred from Pt to CO (0.08 e^-) per CO. In Fig. 13a, the PDOS of the CO molecule is depicted along with that of the Pt(111) slab both before, and after, adsorption showing considerable depletion of *d*-states of Pt near the Fermi level has occurred. At the same time, new bonding (and anti-bonding) orbitals between CO and Pt are created below, and above, the edge, respectively. This results agrees with the previous study of Sautet and Kresse [68]. Figure 13b shows the simulated L edge XANES of Pt with CO and H adsorbed to the surface. Based upon the changes to the PDOS of Pt with CO adsorbed, we ascribe the increase in the absorption edge to hybridization of *d*-orbitals involved in back donation to the CO π-bond. The unfilled anti-bonding orbitals lying in the near Fermi edge region possess some *d* electron character and, therefore, scattering from the 2*p* state is an allowed transition.

Previously Ramaker et al. have interpreted the shape changes 0–5 eV above of the L_3 edge when hydrogen is adsorbed on Pt clusters as a consequence of the formation of Pt–H anti-bonding states [14]. FEFF calculations from Ankudinov et al. [69] follow a similar interpretation for the XANES of K_2PtCl_6. In Fig. 13b, we have calculated the simulated XANES of H on the Pt(111) slab. Adsorption of H produces a similar, but smaller effect than that with adsorbed CO in agreement with the experiments (Fig. 7b). We may also use the simulations to create a ΔXANES spectrum, which shows agreement with the experiments at the L_3 edge as shown in Fig. 13c. The XANES intensity increase above the edge is related to the formation of empty antibonding states above the Fermi level, which are now available.

In addition, this increase in adsorption can be correlated with the catalyst surface area to volume ratio as the smallest particles showed the most dramatic increase in XANES intensity as shown in Figs. 7a and 8. Smaller platinum particles are also known to adsorb CO more strongly than large particles which may lead to higher CO coverages. Catalysts with the largest fraction of surface atoms adsorb more CO (and H_2) per Pt, thus have the largest increases in the XANES. Correlating the XANES intensity increase with the CO coverage has recently been used to estimate surface coverages of CO and H_2O of Au and Pt catalysts under water gas shift conditions [32].

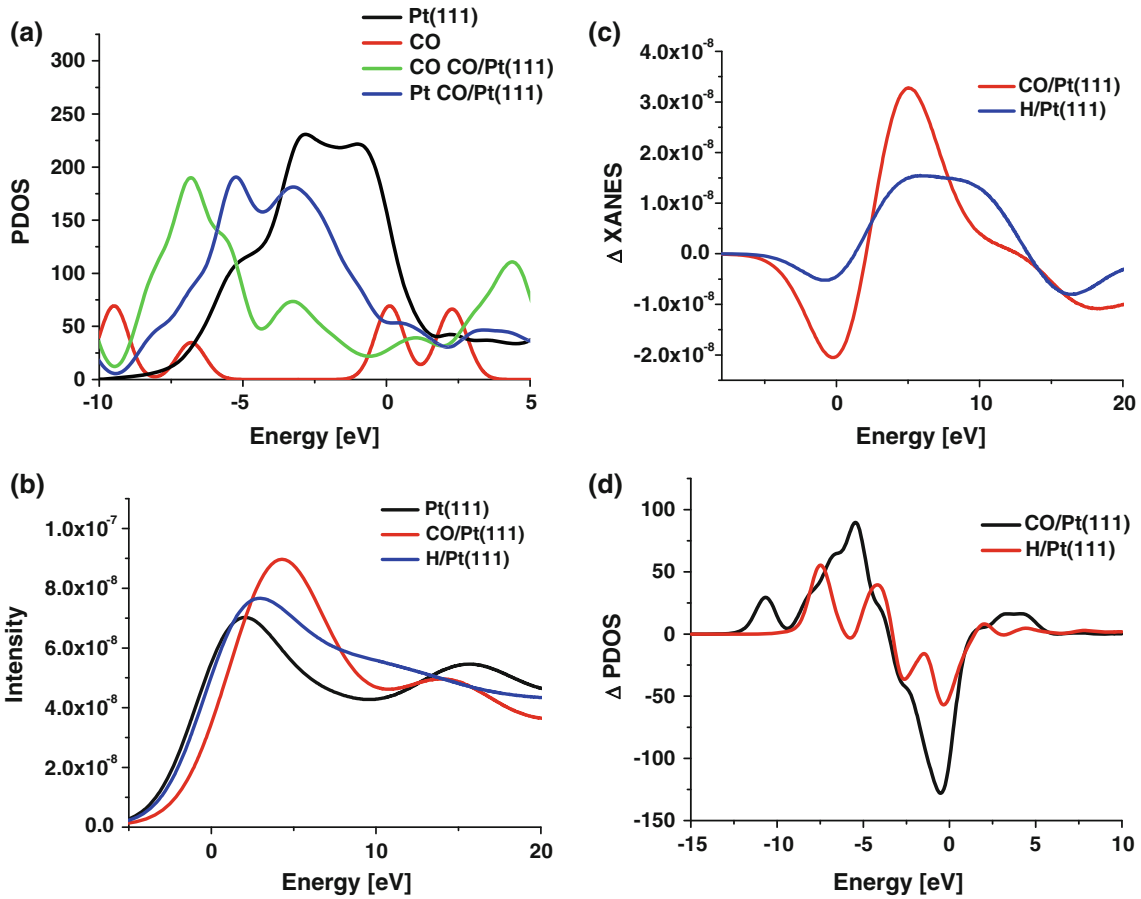

Fig. 13 **a** PDOS of adsorbates on Pt(111). *Green* CO CO/Pt(111). *Blue* Pt CO/Pt(111). *Red* CO. *Black* Pt(111). **b** Simulated XANES of adsorbates on Pt(111). *Blue* H/Pt(111). *Red* CO/Pt(111). *Black* Pt(111). **c** Simulated ΔXANES of adsorbates on Pt(111). *Blue* H/Pt(111). *Red* CO/Pt(111). **d** Simulated ΔPDOS of adsorbates on Pt(111). *Blue* H/Pt(111). *Red* CO/Pt(111)

Although the XANES spectra of CO/Pt(111) and H/Pt(111) have shown an increase in intensity beyond the edge and a shift to higher energies, subtle differences exist. First, the intensity for CO is greater, not surprising due to its stronger bonding and greater depletion of *d*-states as demonstrated in Fig. 13a. Adsorbed hydrogen, on the other hand shows a more diffuse absorption spectra lacking clear features. To better explain this phenomenon, in Fig. 13d, the change in the total PDOS relative to Pt(111) is shown for CO/Pt(111) and H/Pt(111). Two observations can be made. First, the large feature centered around 3.5 eV above the edge gives rise to the increase in XANES intensity due to CO. This state arises from the creation of an anti-bonding orbital between CO and Pt. Second, hydrogen has two features in the PDOS above the edge located at about 2.0 and 4.5 eV. In the XANES spectrum, these features become smeared together, as the ΔXANES of adsorbed hydrogen appears more diffuse. We hypothesize that these features may arise from the interaction of hydrogen the *d* and *sp* states of Pt. It can be noticed that the larger single feature resulting from adsorbed CO also could be convoluted into two peaks but in this case they are closer together. Due to the hybridization in the bonding, the calculation assigns *d* character to these states.

Besides the changes in intensity, shifts in the absorption edges are observed. A simple explanation for the shift would be to ascribe the edge shift to changes in the work function. For example, when CO is adsorbed on Pt(111) the work function is observed to decrease by 240 meV [70]. One would expect, therefore, a shift should to lower binding energy with adsorbates, counter to our experimental observation. Asakura et al. describe the shift as an initial state effect caused by a shift in the location of the $2p$ in response to the adsorption event [27]. However, as Asakura et al. notes if the shift is purely an initial state effect then the L_1 edge should also shift upon hydrogen adsorption, which is not observed experimentally.

In an effort to further understand the increase in edge intensity due to the presence of adsorbates, the orbital resolved PDOS for surface Pt has been calculated both in the absence and presence of CO. We find that the center of the d_{xy} (and $d_{x^2-y^2}$), d_{xz} (and d_{yz}) and d_{z2} orbitals are −2.96, −2.36 and −2.50 eV. When CO is adsorbed, the orbital centers are shifted to −4.22, −4.51 and −4.15 eV

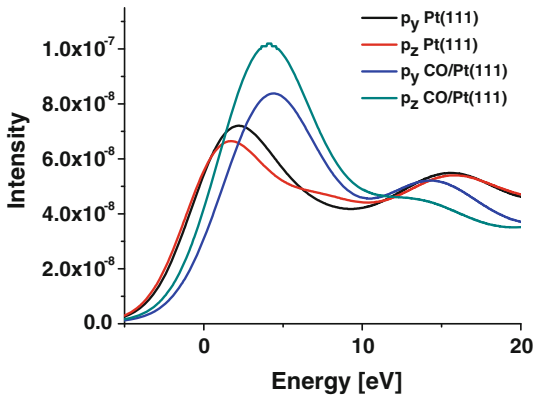

Fig. 14 Simulated XANES comparing transition from p_y and p_z on Pt(111) and CO/Pt(111). *Green* p_z CO/Pt(111). *Blue* p_y CO/Pt(111). *Red* p_z Pt(111). *Black* p_y Pt(111)

respectively. This implies the shifts are 1.26, 2.15 and 1.65 eV. As a complement to this analysis, we have simulated the orbital resolved XANES examining excitation from the $2p_y$ (or $2p_x$) or $2p_z$ as depicted in Fig. 14. By a simple symmetry conservation, we propose that an electron ejected from the p_z can only be scattered into an empty d orbital which possesses some z character (i.e. d_{xz}, d_{yz} and d_{z2}, but not d_{xy} or $d_{x^2-y^2}$). When CO is adsorbed, we see changes between the absorption edges of the p_y and p_z. The XANES intensity of the p_z shows a shift to higher energy and increases dramatically, indicating a high degree of metal-adsorbate bonding (i.e. depletion near the edge and creation of unfilled antibonding orbitals above the edge). The p_y edge shows a larger shift but a smaller intensity increase indicating that orbitals formed involving x and y symmetry are less important to the bonding of CO to the surface. Not surprisingly, this suggests that those orbitals which have z symmetry are more important to the bonding of CO to the surface atoms and therefore the energy level and filling of the d-orbitals with the proper symmetry will control the adsorption (and reactivity).

Previous work of Koningsberger and co-workers has emphasized the role of the support in altering the electronic structure of Pt nanoparticles. However, in our simulations, we do not include the support and yet qualitative trends in the absorption spectra are captured. Furthermore, although we examined a large variety of supports, the trends with regard to particle size and the presence of adsorbates remained, suggesting that any support effects were independent of these variables.

6 Conclusions

DFT calculations has been applied to develop an understanding of experimental XANES spectra the of supported Pt clusters of different size and support composition. Support effects both with respect to lattice parameters and edge intensities were found to be minimal at constant cluster size. As has been observed for other d-band transition metals, the lattice constant of Pt decreased with particle size. In addition, the edge intensity in the L_3 decreased but the intensity increased at the L_2 edge as the particle size decreased, reflecting the changes in hybridization as the coordination and lattice constant decrease with decreasing size. When CO or H_2 was adsorbed, the XANES intensity at the L_3 edge decreases and the edge shifts to higher energy, reflecting the depletion of available states at the Fermi level. Beyond the absorption edge there is an increase in intensity due to the formation of unoccupied molecular orbitals between CO and the metal cluster. Experimentally, much smaller changes occur in the intensity and shift in energy of the L_2 XANES occur with changes in particle size or with adsorbates; however, beyond the edge there are large increase, thought to be due to electronic transition to the Pt-adsorbate anti-bonding orbitals similar to that observed at the L_3 edge. DFT calculations also show that these changes are dependent d orbitals with z symmetry, suggesting that these d orbitals are the ones primarily responsible for adsorbate bonding. In order to fully understand the changes in the XANES spectra, however, it will be necessary to include spin–orbit coupling in the DFT calculations.

Acknowledgments RJM would like to acknowledge the generous grants for computational time on Jazz and Fusion at Argonne National Lab. Use of the Advanced Photon Source is supported by the U. S. Department of Energy, Office of Science, and Office of Basic Energy Sciences, under Contract DE-AC02-06CH11357. MRCAT operations are supported by the Department of Energy and the MRCAT member institutions. In addition, RJM would like to acknowledge the Department of Energy for use of Advanced Photon Source at Argonne National Lab associated with GU-8689. RJM also acknowledges the National Science Foundation for their partial support of this work through CBET grant #0747646. Finally, RJM, JJ and JTM would like to thank Suljo Linic and Hongliang Xin of the University of Michigan for the thoughtful discussions of these results and without whom this work would not have been possible.

References

1. Heiz U, Bullock EL (2004) J Mater Chem 14:564–577
2. Koningsberger DC, Mojet BL, van Dorssen GE, Ramaker DE (2000) Top Catal 10:143–155
3. Ramaker DE, Koningsberger DC (2010) Phys Chem Chem Phys 12:5514–5534
4. Lytle FW, Wei PSP, Greegor RB, Via GH, Sinfelt JH (1979) J Chem Phys 70:4849–4855
5. Short DR, Mansour AN, Cook JW, Sayers DE, Katzer JR (1983) J Catal 82:299–312
6. Ichikuni N, Iwasawa Y (1993) Catal Lett 20:87–95
7. Mansour AN, Cook JW, Sayers DE (1984) J Phys Chem 88:2330–2334
8. Ankudinov AL, Rehr JJ, Low JJ, Bare SR (2002) Top Catal 18:3–7

9. Ankudinov AL, Rehr JJ, Low JJ, Bare SR (2002) J Chem Phys 116:1911–1919
10. Schweitzer N, Xin H, Nikolla E, Linic S, Miller J (2010) Top Catal 53:348–356
11. Lewis PH (1968) J Catal 11:162–174
12. Samant MG, Boudart M (1991) J Phys Chem 95:4070–4074
13. Kubota T, Asakura K, Ichikuni N, Iwasawa Y (1996) Chem Phys Lett 256:445–448
14. Ramaker DE, Mojet BL, Oostenbrink MTG, Miller JT, Koningsberger DC (1999) Phys Chem Chem Phys 1:2293–2302
15. Ankudinov AL, Rehr JJ, Low J, Bare SR (2001) Phys Rev Lett 86:1642–1645
16. Reifsnyder SN, Otten MM, Sayers DE, Lamb HH (1997) J Phys Chem B 101:4972–4977
17. Scott FJ, Mukerjee S, Ramaker DE (2010) J Phys Chem C 114:442–453
18. Roth C, Benker N, Buhrmester T, Mazurek M, Loster M, Fuess H, Koningsberger DC, Ramaker DE (2005) J Am Chem Soc 127:14607–14615
19. Scott FJ, Roth C, Ramaker DE (2007) J Phys Chem C 111:11403–11413
20. Lewis EA, Segre CU, Smotkin ES (2009) Electrochim Acta 54:7181–7185
21. Dimakis N, Iddir H, Diaz-Morales RR, Liu RX, Bunker G, Chung EH, Smotkin ES (2005) J Phys Chem B 109:1839–1848
22. Bus E, Ramaker DE, van Bokhoven JA (2007) J Am Chem Soc 129:8094–8102
23. Teliska A, O'Grady WE, Ramaker DE (2005) J Phys Chem B 109:8076–8084
24. Teliska M, Murthi VS, Mukerjee S, Ramaker DE (2005) J Electrochem Soc 152:A2159–A2169
25. Teliska M, Murthi VS, Mukerjee S, Ramaker DE (2007) J Phys Chem C 111:9267–9274
26. Teliska M, O'Grady WE, Ramaker DE (2004) J Phys Chem B 108:2333–2344
27. Asakura K, Kubota T, Chun WJ, Iwasawa Y, Ohtani K, Fujikawa T (1999) J Synchrotron Radiat 6:439–441
28. Safonova OV, Tromp M, van Bokhoven JA, de Groot FMF, Evans J, Glatzel P (1616) J. Phys Chem B 110(2006):16162–16164
29. Kubota T, Asakura K, Iwasawa Y (1997) Catal Lett 46:141–144
30. Kang JH, Menard LD, Nuzzo RG, Frenkel AI (2006) J Am Chem Soc 128:12068–12069
31. Stoupin S (2009) J Chem Theory Comput 5:1337–1342
32. Guo N, Fingland BR, Williams WD, Kispersky VF, Jelic J, Delgass WN, Ribeiro FH, Meyer R, Miller JT (2010) Phys Chem Chem Phys 12:5678–5693
33. Rioux RM, Hsu BB, Grass ME, Song H, Somorjai GA (2008) Catal Lett 126:10–19
34. Miller JT, Kropf AJ, Zha Y, Regalbuto JR, Delannoy L, Louis C, Bus E, van Bokhoven JA (2006) J Catal 240:222–234
35. Segall MD, Lindan PJD, Probert MJ, Pickard CJ, Hasnip PJ, Clark SJ, Payne MC (2002) J Phys Condens Matter 14: 2717–2744
36. Vanderbilt D (1990) Phys Rev B 41:7892–7895
37. Monkhorst HJ, Pack JD (1976) Phys Rev B 13:5188–5192
38. Perdew JP, Wang Y (1992) Phys Rev B 45:13244–13249
39. Gao SP, Pickard CJ, Perlov A, Milman V (2009) J Phys Condens Matter 21:104203
40. Gao SP, Pickard CJ, Payne MC, Zhu J, Yuan J (2008) Phys Rev B 77:115122
41. Seabourne CR, Scott AJ, Brydson R, Nicholls RJ (2009) Ultramicroscopy 109:1374–1388
42. Feibelman PJ, Hammer B, Norskov JK, Wagner F, Scheffler M, Stumpf R, Watwe R, Dumesic J (2001) J Phys Chem B 105:4018–4025
43. Kumar V, Kawazoe Y (2008) Phys Rev B 77:205418
44. Hu CH, Chizallet C, Mager-Maury C, Corral-Valero M, Sautet P, Toulhoat H, Raybaud P (2010) J Catal 274:99–110
45. Vaarkamp M, Miller JT, Modica FS, Koningsberger DC (1996) J Catal 163:294–305
46. Nepijko SA, Klimenkov M, Adelt M, Kuhlenbeck H, Schlogl R, Freund HJ (1999) Langmuir 15:5309–5313
47. Vila F, Rehr JJ, Kas J, Nuzzo RG, Frenkel AI (2008) Phys Rev B 78:121404
48. Tew MW, Miller JT, van Bokhoven JA (2009) J Phys Chem C 113:15140–15147
49. Williams MF, Fonfe B, Woltz C, JentyS A, van Veen JAR, Lercher JA (2007) J Catal 251:497–506
50. Ramallo-Lopez JM, Santori GF, Giovanetti L, Casella ML, Ferretti OA, Requejo FG (2003) J Phys Chem B 107:11441–11451
51. Stakheev AY, Zhang Y, Ivanov AV, Baeva GN, Ramaker DE, Koningsberger DC (2007) J Phys Chem C 111:3938–3948
52. Nikolla E, Schwank J, Linic S (2009) J Am Chem Soc 131: 2747–2754
53. Muller DA, Singh DJ, Silcox J (1998) Phys Rev B 57:8181–8202
54. Ching WY, Rulis P (2009) J Phys Condens Matter 21:104202
55. Keast VJ, Scott AJ, Brydson R, Williams DB, Bruley J (2001) J Microsc 203:135–175
56. Muller DA (1998) Phys Rev B 58:5989–5995
57. Hammer B (2006) Top Catal 37:3–16
58. Hammer B, Norskov JK (2000) Adv Catal 45:71–129
59. Zhao Y, Feltes TE, Regalbuto JR, Meyer RJ, Klie RF (2010) J Appl Phys 108:063704
60. Ankudinov AL, Nesvizhskii AI, Rehr JJ (2001) J Synchrotron Radiat 8:92–95
61. van Bokhoven JA, Miller JT (2007) J Phys Chem C 111: 9245–9249
62. Mason MG (1983) Phys Rev B 27:748–762
63. Bus E, van Bokhoven JA (2007) J Phys Chem C 111:9761–9768
64. Richter B, Kuhlenbeck H, Freund HJ, Bagus PS (2004) Phys Rev Lett 93:026805
65. Boyanov BI, Morrison TI (1996) J Phys Chem 100:16318–16326
66. Blyholder G (1964) J Phys Chem 60:2772–2778
67. Henkelman G, Arnaldsson A, Jonsson H (2006) Comput Mater Sci 36:354–360
68. Kresse G, Gil A, Sautet P (2003) Phys Rev B 68:073401
69. Ankudinov AL, Rehr JJ, Bare SR (2000) Chem Phys Lett 316:495–500
70. Poelsema B, Palmer RL, Comsa G (1982) Surf Sci 123:152–164